Optimizing Black Phosphorus/Halide Perovskite Compositions by Scanning Photoelectrochemical Microscopy

Journal of The Electrochemical Society, 2022 **169** 096510
1945-7111/2022/169(9)/096510/6/$40.00 © 2022 The Electrochemical Society ("ECS"). Published on behalf of ECS by IOP Publishing Limited

Optimizing Black Phosphorus/Halide Perovskite Compositions by Scanning Photoelectrochemical Microscopy

Rugeng Liu,[1,2,3,=] Jiahong Wang,[4,5,=] Chun Hong Mak,[1,2,3,=] Minshu Du,[6] Fang-Fang Li,[7] Hsin-Hui Shen,[8] Shella Permatasari Santoso,[9] Edward T. Yu,[10] Xuefeng Yu,[5] Paul K. Chu,[2,4,z] and Hsien-Yi Hsu[1,2,3,z]

[1]*School of Energy and Environment, City University of Hong Kong, Kowloon Tong, Hong Kong, People's Republic of China*
[2]*Department of Materials Science and Engineering, City University of Hong Kong, Kowloon, Hong Kong, People's Republic of China*
[3]*Shenzhen Research Institute of City University of Hong Kong, Shenzhen 518057, People's Republic of China*
[4]*Department of Physics City University of Hong Kong, Kowloon, Hong Kong, People's Republic of China*
[5]*Shenzhen Institute of Advanced Technology, Chinese Academy of Sciences, Shenzhen, People's Republic of China*
[6]*School of Materials Science and Engineering, Northwestern Polytechnical University, Xi'an, Shaanxi 710072, People's Republic of China*
[7]*School of Materials Science and Engineering, Huazhong University of Science and Technology, 1037 Luoyu Road, Wuhan 430074, People's Republic of China*
[8]*Department of Materials Science and Engineering, Faculty of Engineering, Monash University, Clayton, VIC 3800, Australia*
[9]*Chemical Engineering Department, Widya Mandala Surabaya Catholic University, East Java, Indonesia*
[10]*Microelectronics Research Center, Department of Electrical and Computer Engineering, The University of Texas at Austin, Austin, Texas 78758, United States of America*

The incorporation of black phosphorus (BP) into methylammonium lead iodide ($MAPbI_3$) perovskites has been investigated and optimized by a high throughput screening method using scanning photoelectrochemical microscopy (SPECM) to determine how the addition of BP affects its photoelectrochemical and photovoltaic properties. An optimum ratio of 2.0 mole% BP/$MAPbI_3$ perovskite composite generates an increased photocurrent response compared to pristine $MAPbI_3$ for 2 mM benzoquinone (BQ) reduction at −0.6 V vs $Ag/AgNO_3$ on a spot array electrode under illumination. Due to the relatively high quantum yield of $MAPbI_3$, time-resolved photoluminescence measurements have been conducted to investigate photophysical behaviors of BP/$MAPbI_3$ composites. The optimal 2.0 mole% BP/$MAPbI_3$ exhibits an increased electron-hole diffusion lifetime compared to the pristine $MAPbI_3$ perovskite. Finally, we demonstrate the enhanced efficiency and stability of 2.0% BP/$MAPbI_3$-based perovskite solar cells arising from impeded Pb^0-defect generation and suppressed charge-carrier recombination.
 [DOI: 10.1149/1945-7111/ac8d34]

Manuscript submitted July 13, 2022; revised manuscript received August 23, 2022. Published September 7, 2022.

Supplementary material for this article is available online

Lead-based halide perovskites show remarkable properties, consisting of wide absorption range, long exciton diffusion lengths, facile solution-based process, and low exciton binding energies,[1–6] achieving power conversion efficiencies (PCE) of ∼25.7% in perovskite solar cells.[7] In addition to the cost of large-scale production, the key bottleneck for the commercialization of PSCs is their stability, because typical lead-based perovskites, e.g., methyl ammonium lead iodide ($MAPbI_3$), are extremely sensitive to oxygen and moisture.[8–12] It has been reported that long-term stability of organic–inorganic halide perovskite-based photovoltaic devices could be improved by the stability of electron/hole transport layers and halide perovskite materials.[13–18] On the other hand, the charge-carrier recombination of perovskite-based light absorbers not only degrades the stability of perovskite materials but also reduces the performance of photovoltaic devices. Such effects occur because metallic Pb^0 has been formed by the reduction of Pb^{2+} induced by photothermal effect in addition to the irreversible degradation.[19,20]

Two-dimensional (2D) black phosphorous (BP) with high hole mobility has been recognized as an efficient hole injection layer for application in perovskite-based light-emitting diode (PeLED) and perovskite-based photovoltaic devices.[21–23] On the basis of theoretical investigations, it has been suggested that BP shows a unique self-repairing characteristic, leading to the suppression of chare-carrier recombination.[24,25] For electrical applications, charge recombination has been substantially reduced by the use of BP.[26] However, the optimization of BP-incorporated halide perovskite compositions is time-consuming. Accordingly, determining optimal ratio of BP to halide perovskite for optoelectronic and photovoltaic performance is of considerable interest. Building on the discovery of stable electrolytes in the dichloromethane system,[1,27,28] scanning photoelectrochemical microscopy (SPECM) combined with combinatorial synthesis offers a high-throughput screening approach for newly developed halide perovskite composites on photoelectrode arrays. In this report, we use this approach to screen a series of BP-incorporated $MAPbI_3$ perovskite composites efficiently using the SPECM imaging technology. By using time-resolved photoluminescence, the longest exciton diffusion lifetime (∼0.136 μs) of optimized 2.0 mole% BP/$MAPbI_3$ perovskite composites has been demonstrated, giving rise to the most efficient power conversion efficiency of 19.112%. Improved stability of 2.0% BP/$MAPbI_3$ perovskite solar cells has also been verified by the evaluation of photovoltaic performance.

Experimental

Chemicals.—Based on our previous experiences,[27,28] methylamine (CH_3NH_2, 2 M in methanol, Alfa Aesar), hydroiodic acid (HI, 57 wt% in water, Alfa Aesar), lead iodide (PbI_2, 99.9985% metals basis, Alfa Aesar), black phosphorus (BP) was purchased from Nanjing XFNANO Materials Tech. Co., Ltd. Phenyl-C 61 -butyric acid methyl ester (PCBM; Solenne BV), poly(N,N′-bis-4-butylphenyl-N,N′-bisphenyl)benzidine (poly-TPD, Xi'an Polymer Light Technol. Corp.), Poly[2-methoxy-5-(2-ethylhexyloxy)−1,4-phenylenevinylene] (MEH-PPV, Xi'an Polymer Light Technol. Corp.) N,N-dimethylformamide (DMF, ⩾99.9%, Sigma-Aldrich), methylene chloride (CH_2Cl_2, anhydrous, ⩾99.9%, Sigma-Aldrich), Tetrahydrofuran (THF, anhydrous, ⩾99.9%, Sigma-Aldrich), ethyl

=Equal Contribution.
zE-mail: paul.chu@cityu.edu.hk; sam.hyhsu@cityu.edu.hk

acetate (EA, anhydrous, ⩾99.8%, Sigma-Aldrich), dimethyl sulfoxide (DMSO, ⩾99.9%, Sigma-Aldrich), chlorobenzene (CB, ⩾99.9%, Sigma-Aldrich), toluene (⩾99.9%, Sigma-Aldrich), *p*-Benzoquinone (BQ, ⩾99.5%, Sigma-Aldrich), Tetrabutylammonium hexafluorophosphate ($TBAPF_6$, ⩾99.9%, Sigma-Aldrich). FTO-coated glass was obtained from Pilkington (Toledo, OH) as a substrate of the electrodes. The 15 × 15 mm squares were cleaned by successive sonication in ethanol and 2-propanol and rinsed with deionized water.

Preparation of perovskite composite film.—According to our published literature,[27] p-$MAPbI_3$ was spin-cast on indium tin oxide (ITO) glass substrates from N,N-dimethylformamide (DMF) (Alfa Aesar) solution with the mixture of MAI and PbI_2. MAI was synthesized by stirring 27.86 ml methylamine (2 M in methanol, Alfa Aesar) and 30 ml of hydroiodic acid (57 wt% in water, Alfa Aesar) in 250 ml round bottomed flask in an ice bath under an argon atmosphere for 3 h. After the reaction, the solvent was evaporated using a rotary evaporator. A white powder, methyl ammonium iodide (MAI), was washed with diethyl ether by stirring the solution for 30 min, which was repeated three times, and then finally dried at 60 °C in vacuum oven for 24 h.[29] The synthesized MAI white powder was mixed with PbI_2 (Alfa Aesar) in DMF at 100 °C for one hour.[30] The mole percent of BP to $MAPbI_3$ was increased in the order of 0%, 2.0%, 4.0%, 6.0%, 8.0%, and 10.0% for preparing a series of BP/ $MAPbI_3$ composites.

Material characterization.—A CH Instruments Model 760E electrochemical analyzer (Austin, TX) was used as a potentiostat for the experiments with the thin film electrodes. Illumination was with a Xenon lamp (XBO 150 W, Osram) at full output for UV–visible irradiation. Glancing incidence angle X-ray diffraction (XRD) measurements were performed by using D8 ADVANCE (Bruker, Fitchburg, WI) equipped with a Cu Kα radiation source where the incident angle was 0.4°. The film thickness was measured by scanning electron microscopy (SEM, Quanta 650 FEG, FEI Company, Inc., Hillsboro, OR). The ultraviolet-visible (UV–vis) absorption spectra were obtained by using a UV–vis spectrophotometer (SHIMADZU, UV-2600, Kioto, Japan). The photoluminescence (PL) spectra were recorded by a spectrofluorometer (SHIMADZU, RF-5301PC, Kioto, Japan). The current-voltage characteristics of the devices were monitored with a Keithley 2400 source meter under one sun illumination (AM 1.5 G, 100 mW cm^{-2}) or under dark. The external quantum efficiency (EQE) measurements were carried out on the home-built setup. To examine the surface roughness, the films were characterized by atomic force microscope (AFM) (MultiMode 8-HR, Bruker, USA).

Preparation of spot array electrodes.—Spot array electrodes (an electrode composed of spots with each spot having a different composition) were fabricated using a previously reported method[31] using a CH Instruments dispenser. For precursor dispensing, a CH Instruments model 1550 dispenser (Austin, TX) with a piezoelectric dispensing tip (Micro Jet AB-01–60, MicroFab, Plano, TX) connected to an XYZ stage driven by a computer-controlled stepper-motor system (Newport) was used. The precursor solutions (0.518 M in DMF) comprising PbI_2, MAI, and different amounts of BP, were dispensed in a preprogrammed pattern onto the ITO substrate. In all cases, the ratio of BP-to-$MAPbI_3$ compositions was controlled from 0 to 10 mole% of. The prepared arrays were annealed at 100 °C for 1 h in air to form the $MAPbI_3$ perovskites.

Screening the spot array electrodes.—A schematic SECM setup has been described previously.[31] Briefly, a 400 μm diameter optical fiber was connected to a 150 W xenon lamp (Oriel) and was attached to the tip holder of a CHI 900B SECM. A 420 nm long-pass filter (removing the UV portion of the spectrum) was used for visible light only illumination in rapid screening experiments. The perovskite array was used as the working electrode and was placed in the bottom of a custom designed Teflon SECM cell with an O-ring (exposed area: 1.0 cm^2). A Pt wire was used as the counter electrode, and a saturated $Ag/AgNO_3$ electrode was used as the reference electrode. The electrolyte consisted of 2 mM BQ and 0.1 M $TBAPF_6$ (supporting electrolyte). Light from the xenon lamp was passed through the optical fiber, positioned perpendicular to the working electrode ~200 μm above the surface, to illuminate one spot on the working electrode at a time. The optical fiber tip was scanned across the spot array electrode with a scan rate of 500 μm s^{-1}, while a potential of −0.6 V vs $Ag/AgNO_3$ was applied to the working electrode through the SECM potentiostat. Scanning over the spot arrays revealed two-dimensional images indicative of the generation of photocurrent on each spot.

Photoelectrochemical measurements.—The results on array electrodes were confirmed by photoelectrochemical (PEC) responses measured for perovskite and perovskite composite films in a photoelectrochemical cell. The perovskite composite films were used as working electrodes (0.27 cm^2) exposed to electrolyte solution and simulated solar illumination. All measurements were carried out in a borosilicate glass cell with a carbon counter electrode and $Ag/AgNO_3$ reference electrode (a silver wire immersed in 0.01 M silver nitrate in MeCN connected to the cell via a 0.10 M $TBAPF_6$ in deaerated CH_2Cl_2 salt bridge).[1] All potentials are reported vs $Ag/AgNO_3$ in deaerated CH_2Cl_2. Illumination was provided through the electrolyte solution using the full output of a Xe lamp with an incident light intensity of about 100 mW cm^{-2}. The supporting electrolyte was 0.1 M $TBAPF_6$ in deaerated CH_2Cl_2.

Device fabrication.—The photovoltaic devices have been prepared based on the literature.[32] The indium tin oxide (ITO) glasses were cleaned by deionized water, and then dried them in an oven. Prior to the fabrication of solar cells, ITO glasses were first treated with a UVO cleaner with the model of 144A-220 at Jelight Co. Inc. for 20 min. For the formation of a thin HTM layer, the poly-TPD (4 mg ml^{-1} in CB) or MEH-PPV (4 mg ml^{-1} in CB) solution was then spin-coated on the surface of ITO conductive glassed at 5000 and 3000 rpm for 35 s, respectively, followed by annealing at 100 °C for 15 min. The HTM layer was then treated by a UVO cleaner with the time period of ~30 s. Afterwards, pure perovskite and BP/ perovskites composite films were deposited on the top of the HTM layer by a one-step spin-coating method. In the spin-coating process, the substrate was treated by toluene using drop-casting technique. Eventually, the precursor layers were annealed at 100 °C for 10 min. Subsequently, we used a thermal evaporation to deposit a 20 nm thick fullerene (C60) layer, a 5 nm-thick 2, 9-dimethyl-4,7-diphenyl-1,10-phenanthroline (BCP) layer and Ag electrode (80 nm) successively.

Results and Discussion

SPECM scanning of perovskite arrays.—It has been reported that materials such as semiconductors and catalysts could be effectively screened by scanning electrochemical microscopy (SECM).[33–35] In our photoelectrode arrays, the diameter of each semiconductor spot is approximately 350 μm. The semiconductor composites were deposited on a conductive glass substrate utilizing a piezoelectric dispenser. For photoactive semiconductors, we modified a typical SECM system by replacing the conventional working electrode with an optical fiber, as illustrated in Fig. 1a. During the optimization process, we can reduce the use of precursor materials by this combinatorial screening technology[36,37] for directly monitoring PEC activities on different elements of the photoelectrode array.[38] By combining SPECM with time-resolved photoluminescence (TRPL) measurements on different molar ratios of $BP/MAPbI_3$ halide perovskite composites, the cause-and-effect relationship between material compositions and PEC responses could be clarified by a combination of the SECM imaging technology and photoluminescence decay dynamics.

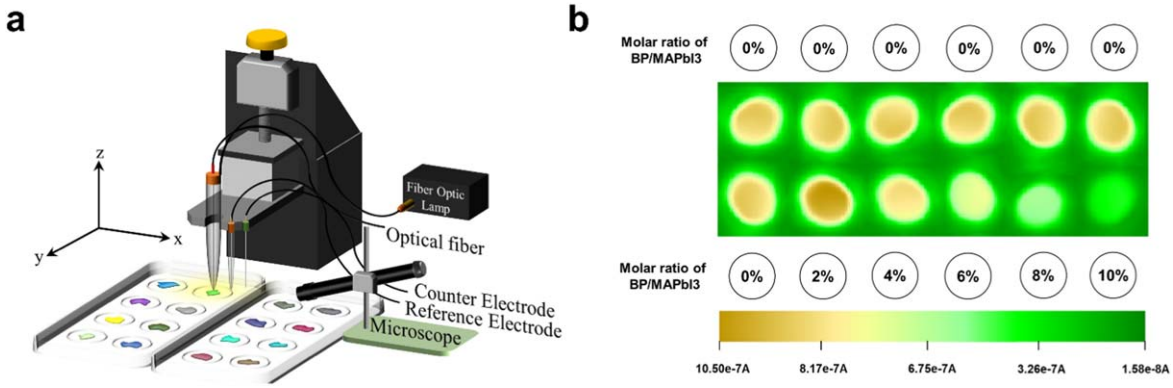

Figure 1. (a) Modified SPECM setup equipped with an optical fiber as a screening tip. (b) SPECM images with PEC responses of $BP/MAPbI_3$ halide perovskite composites under visible-light illumination. The colorful scale bar in the SPECM image denotes the produced photocurrents on the semiconductor spots. In the upper six-spot rows, they are pristine $MAPbI_3$ halide perovskites. The lower six-spot row represents different molar ratio of BP incorporated in the $MAPbI_3$ halide perovskites in the array photoelectrode. To collect the SPECM image, we employed 2 mM $BQ/BQ^{-\bullet}$ redox couple and 0.1 M $TBAPF_6$ supporting electrolytes in CH_2Cl_2 under an applied potential of −0.6 V vs $Ag/AgNO_3$.

It has been reported previously that the addition of BP into $MAPbI_3$ halide perovskites can possibly enhance the photocurrent density.[39] However, the optimal amount of BP incorporated in $MAPbI_3$ still remains unknown. Through a rapid screening using SPECM, we can efficiently determine the optimum ratio of $BP/MAPbI_3$ halide perovskite composites. We employed the SECM system to screen the $BP/MAPbI_3$-based array photoelectrodes, detecting the photocurrent response on the compositions of $MAPbI_3$ doped with a series of BP ranging from 0 mole% to 10 mole %. As shown in Fig. 1b, 2.0 mole% of BP to $MAPbI_3$ exhibited the highest photocurrent under visible-light illumination. The photocurrents were lower compared to the pure $MAPbI_3$ for molar ratios of $BP/MAPbI_3$ of 4.0% or higher. As depicted in Fig. 1b, the SECM image of a spot array photoelectrode consisting of $BP/MAPbI_3$ halide perovskite compositions has been conducted under illumination. In Fig. 1b, the colors denote the photocurrent magnitude produced by the reduction reaction of BQ/BQ^- redox couples under an applied potential of −0.6 V vs $Ag/AgNO_3$. The brown color represents higher photocurrents, while the green represents lower photocurrents. In the SPECM image, there are two rows and six columns of spots in the array photoelectrode. In order to verify the reproducibility, the first six-spot row contains only pure $MAPbI_3$ halide perovskites, for which all the photocurrents are almost the same (∼0.81 ± 0.03 μA). On the second six-spot row, the leftmost spot is denoted as the pristine $MAPbI_3$. Moving to the right in the second row, each spot represents an increased molar ratio of $BP/MAPbI_3$ halide perovskite composites, as illustrated in the SECM image of Fig. 1b. The averaged photocurrent of the 2.0% $BP/MAPbI_3$ perovskite composite is ∼1.02 μA, while the pristine $MAPbI_3$ perovskite generates a photocurrent of ∼ 0.82 μA.

Material characterization and photoelectrochemical responses.—A one-step deposition and annealing process has been used to make the pristine $MAPbI_3$ perovskite and prepare $BP/MAPbI_3$ composites by varying the amount of BP in the solution with PbI_2 and MAI precursors. The X-ray diffraction (XRD) spectra of $BP/MAPbI_3$ composition films have also been measured. For 0 mole% $BP/MAPbI_3$ composites, only the β-phase of the pristine $MAPbI_3$ perovskite is observed (Fig. 2a).[40] The XRD patterns of $MAPbI_3$ composites incorporating different amounts of BP are essentially identical, which is in accordance with the previous report.[39] The thin-film bulk photoelectrodes of the pure $MAPbI_3$ and $BP/MAPbI_3$ perovskite composites were then characterized by their PEC responses to validate the experimental results of the SPECM images. By using linear sweep voltammetry (LSV) under chopped-light illumination, the photocurrent densities of $BP/MAPbI_3$ perovskite composites with the molar ratio ranging from 0% to 10.0% were obtained, as shown in Fig. 2b. The LSV measurements were measured with the potentials scanned from +0.40 to −0.60 V vs $Ag/AgNO_3$ at a scan rate of 50 mV s^{-1}. The 2.0% and 10.0% $BP/MAPbI_3$ composite photoelectrodes produced photocurrents of 6.2×10^{-5} A and 0.4×10^{-5} A at−0.6 V vs $Ag/AgNO_3$ for the reduction reaction of BQ/BQ^- redox couples, while the pure $MAPbI_3$ perovskite generated a photocurrent of $\sim 4.1 \times 10^{-5}$ A. These PEC results obtained by LSV are in accordance with those of the SPECM image in c 1b, thereby demonstrating the validity of using SECM imaging technology for the determination of PEC performance on $BP/MAPbI_3$ halide perovskite composites. As shown in Fig. 3, the addition of BP into the $MAPbI_3$ perovskites also affects the surface morphology, with SEM images revealing that pure $MAPbI_3$ perovskites and 2.0% $BP/MAPbI_3$ composites exhibit full coverage and pinhole-free thin films with the average grain size of ∼250 nm. However, the grain size of the 4.0% $BP/MAPbI_3$ samples become smaller (∼180 nm) while some defects or impurities of 6.0%, 8.0%, and 10.0% $BP/MAPbI_3$ samples are observed, and correspond to decreased PEC responses as measured by LSV. We have also performed the surface roughness analysis of different $BP/MAPbI_3$ composites to quantitatively investigate the smoothness of the perovskite film surface using AFM. All the films (0% to 6% $BP/MAPbI_3$) were measured in the scanning areas of 10×10 μm^2 (Fig. S1 (available online at stacks.iop.org/JES/169/096510/mmedia)). At least six scanning areas of the film were randomly measured. The average roughness and the root mean square roughness are listed in Table A·II. From the statistical and imaging results, 2% $BP/MAPbI_3$ composites film exhibit excellent parameters of the roughness test (i.e., lowest roughness average and root mean square roughness of 10.82 nm and 13.65 nm, respectively).

Photophysical property and decay dynamics.—UV–vis absorption spectra of pure $MAPbI_3$ and $BP/MAPbI_3$ composite perovskites have also been measured (Fig. 4a). The absorption edges of both $MAPbI_3$ and $BP/MAPbI_3$ films are located at ∼780 nm, which is the same with that of a typical single-phase $MAPbI_3$ perovskite. The absorptivity of the 2.0 mole% $BP/MAPbI_3$ composites is higher than that of pure $MAPbI_3$ perovskites due to the incorporation of BP into $MAPbI_3$. The poor film quality for $BP/MAPbI_3$ composites with molar ratios of 4.0 mole% or higher leads to reduced absorptivity in the range from 350 nm to 600 nm. The steady-state photoluminescence (PL) spectra for perovskite composite films have been measured with an excitation wavelength of 450 nm under ambient conditions (Fig. 4b). The $MAPbI_3$ and $BP/MAPbI_3$ composite films exhibit a strong PL peak at ∼775 nm. To establish carrier lifetime parameters, we measured PL decay dynamics for $BP/MAPbI_3$ perovskite composite films with and without the addition of BP.[41] By using a time correlated single photon counting (TCSPC) system, we collected time-resolved photoluminescence (TRPL) spectra of

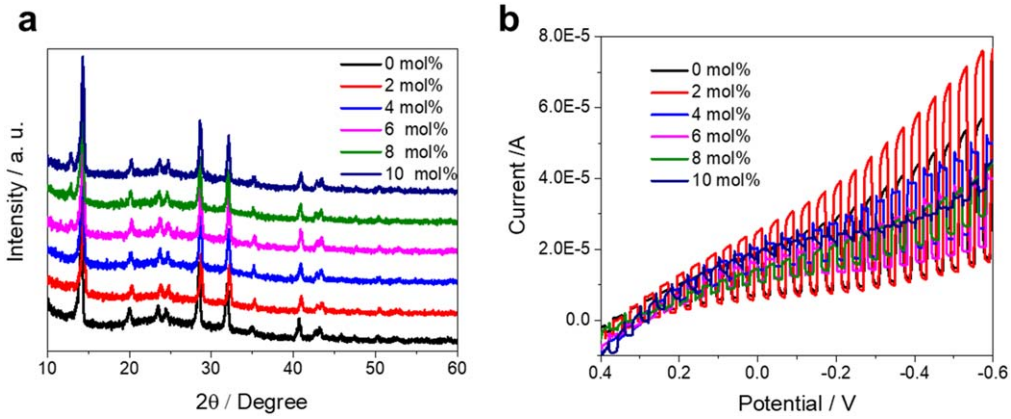

Figure 2. (a) X-ray diffraction (XRD) patterns of a series of BP-incorporated $MAPbI_3$ composite films. (b) The photocurrent densities of bulk film electrodes, including 0% BP/$MAPbI_3$ (black), 2.0% BP/$MAPbI_3$ (red), 4.0% BP/$MAPbI_3$ (blue), 6.0% BP/$MAPbI_3$ (magenta), 8.0% BP/$MAPbI_3$ (olive), and 10.0% BP/$MAPbI_3$ (navy), measured using linear sweep voltammetry (LSV) under 100 mW cm^{-2} chopped-light illumination at a scan rate of 50 mV s^{-1}. The photocurrent is produced by the reduction of $BQ/BQ^{-\bullet}$ redox couples with 0.1 M $TBAPF_6$ as the supporting electrolyte in CH_2Cl_2 (counter electrode: Pt; reference electrode: $Ag/AgNO_3$).

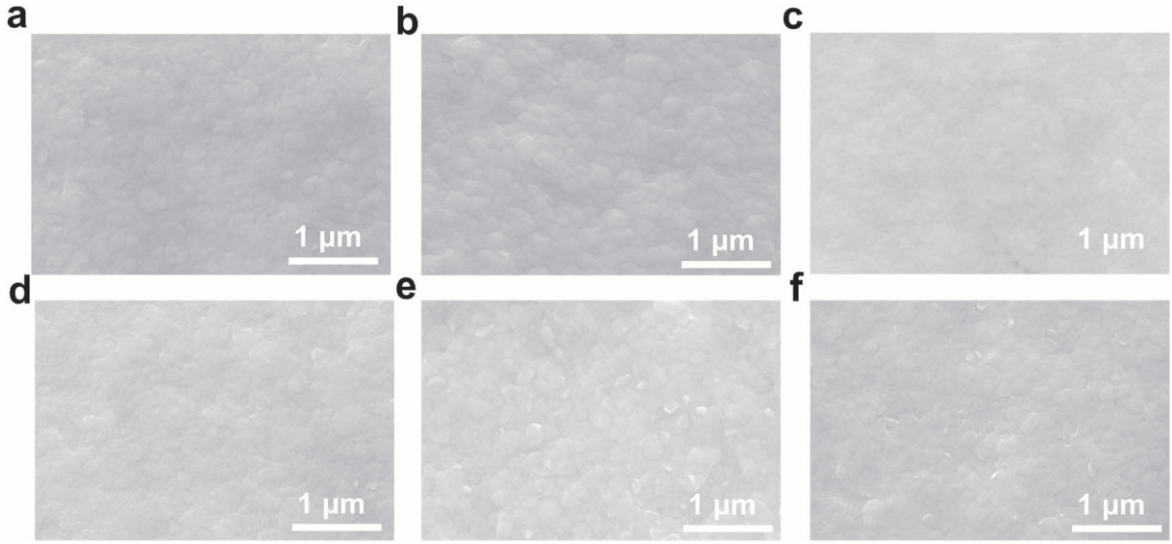

Figure 3. SEM images of BP/MAPbI3 composite perovskites with the BP-to-$MAPbI_3$ molar ratio of (a) 0%, (b) 2.0%, (c) 4.0%, (d) 6.0%, (e) 8.0%, (f) 10.0%.

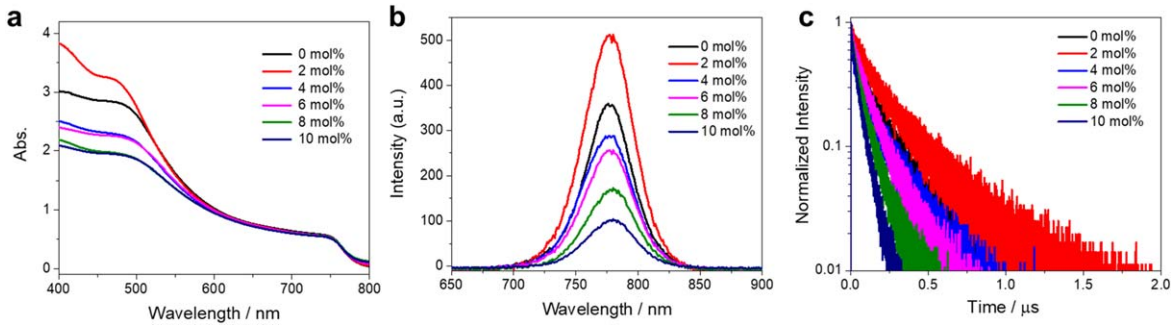

Figure 4. (a) UV–vis absorption, (b) steady-state photoluminescence, and (c) time-resolved photoluminescence spectra of different molar ratios of BP/$MAPbI_3$ films under excitation at 450 nm.

BP/$MAPbI_3$ perovskite composite films to examine the PL decay dynamics. For the TRPL measurements, we utilized a pulsed laser with the excitation wavelength of 450 nm, which could provide $<$ 200 ps pulses with the fluence of $\sim$30 nJ cm^{-2}.[41] BP/$MAPbI_3$ perovskite films with thicknesses of about 200 nm have been used for the photophysical characterizations because this film thickness is close to the typical thickness in photovoltaic and optoelectronic devices. We monitored PL emissions at $\sim$775 nm to determine the PL decay dynamics of those perovskite composite films (Fig. 4c). By fitting PL decay curves using exponential functions, the PL decay lifetime, τ_{PL}, was then estimated (Table A·I).[41,42] We have summarized the fitting lifetimes and corresponding amplitudes (τ_1, $\square_1$, τ_2, $\square_2$) of PL decay curves in Table A·I. The fast decay component, τ_1, of the pristine $MAPbI_3$ perovskite, i.e., 0% BP/$MAPbI_3$, exhibits a

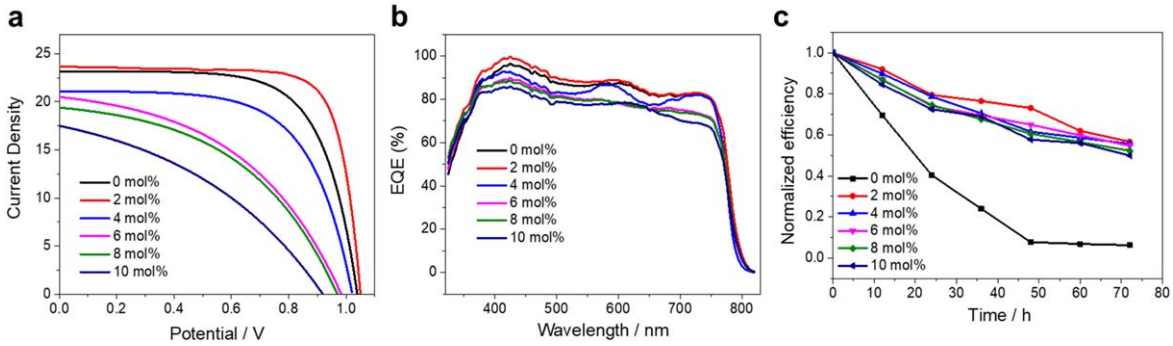

Figure 5. (a) *J-V* characteristics of perovskite solar cells based on $MAPbI_3$ with different amounts of BP under simulated AM 1.5 G solar illumination of 100 mW·cm^{-2}. (b) EQE spectra of as-prepared BP/$MAPbI_3$-based perovskite solar cells. (c) Stability test of encapsulated perovskite solar cells based on $MAPbI_3$ with different concentration of BP.

time constant of $\tau_1 = 0.052$ μs, probably because of bimolecular recombination;[43–45] on the other hand, its long decay component, with lifetime τ_2, is assigned to free carrier recombination in the radiative relaxation process, which is in agreement with the PL decay of $MAPbI_3$ films in the published literature.[41,46] For 2.0 mole % BP/$MAPbI_3$ perovskite composite films, the overall photoluminescence lifetime τ_{PL} was largest, at 0.136 μs, which we attribute to the incorporation of BP into $MAPbI_3$ perovskite films leading to reduced charge-carrier recombination. The electronic defects produced at grain boundaries of the pure $MAPbI_3$ perovskite film give rise to increased charge-carrier recombination, yielding the relatively lower photocurrent density shown in Fig. 1b and a shorter photoluminescence lifetime $\tau_{PL} = 0.104$ μs. By comparison, photoluminescence lifetimes τ_{PL} for 4.0 mole% and 6.0 mole% of BP/$MAPbI_3$ perovskite composite films are significantly shorter, at 0.071 μs and 0.061 μs, respectively, since the BP might dominate crystal phases in the perovskite composite films.[47] By adding 8.0 mole% and 10.0 mole% of BP into $MAPbI_3$ perovskite film, their lifetimes are then reduced further to $\tau_{PL} = 0.048$ μs and 0.034 μs since the BP at higher BP-to-$MAPbI_3$ ratios functions as a hole quencher layer instead of a passivation layer.[48]

Photovoltaic performance.—The results of material and photophysical characterizations reveal that the incorporation of BP can potentially enhance the performance of $MAPbI_3$-based photovoltaic devices. We then fabricated the inverted perovskite solar cells with poly-TPD as a hole transport layer and C60 as an electron transport layer. Figure 5a shows the measured photovoltaic performance characteristics of a series of BP/$MAPbI_3$-based solar cells, as summarized in Table I. In comparison to pristine $MAPbI_3$ perovskites, the 2.0 mole% BP/$MAPbI_3$-based solar cell shows the best power conversion efficiency (PCE) of 19.112% with a short-circuit current density (J_{sc}) of 23.70 mA cm^{-2}, an open-circuit voltage (V_{oc}) of 1.05 V, and a fill factor (*FF*) of 0.768. The PCE of other BP/$MAPbI_3$ composite-based PSCs (i.e., 4.0, 6.0, 8.0, 10.0 mole% BP) show a decreasing trend in performance with increasing BP mole fraction, resulting from a combined effect including poorer surface morphology, lower light absorptivity, and more charge-carrier recombination. The external quantum efficiency (EQE) spectra have been measured and plotted in Fig. 5b. They reach the maximums at $\sim$ 425 nm and moderately decrease at the longer wavelength. The integrations of EQE spectra are good agreement with the photocurrent density evaluated by using the solar simulator. As reported in the published literature,[49,50] the self-healing property of BP is possibly beneficial for the stability of perovskite solar cells. Therefore, we evaluated the stability of as-prepared BP/$MAPbI_3$-based perovskite solar cells with a representative inverted planar configuration of ITO/poly-TPD/perovskite composite/C_{60}/BCP/Ag. Figure 5c shows the normalized power conversion efficiency of unencapsulated BP/$MAPbI_3$-based perovskite solar cells under ambient conditions. Compared with the pure $MAPbI_3$ counterpart, the BP/$MAPbI_3$-based perovskite solar cells show improved stability under continuous 100 mW cm^{-2} illumination. The photovoltaic efficiency of pure $MAPbI_3$-based PSCs dramatically declined to less than $\sim$10% of the initial PCE after continuous 50 h illumination (Fig. 5c) The BP-incorporated $MAPbI_3$-based perovskite solar cells retain $\sim$50%–67% of their original solar efficiency after continuous 72 h illumination, as shown in Fig. 5c.

Conclusions

The SPECM imaging technique employing an optical fiber as a screening tip has been used to optimize the incorporation of BP into $MAPbI_3$ perovskite composites for photovoltaic applications. We demonstrate that 2.0 mole% BP/$MAPbI_3$ exhibits higher light absorptivity, stronger PEC response, longer carrier lifetime, enhanced power conversion efficiency, and improved photovoltaic stability as a result of the compact surface morphology, a self-repairing characteristic, and suppressed charge-carrier recombination of the incorporated BP elements. We believe the SPECM imaging technique is the potential to perform operando photoelectrochemical analysis. For example, the operando SPECM microscopy technique can map out the electrochemical redox activity of perovskite materials. In addition, the electrochemically inactive defect sites on the perovskite film can also be investigated. Consequently, the utilization of this high-throughput screening apparatus opens up an avenue to effectively develop and optimize next-generation semiconductor materials for practical applications in the emerging field of energy-saving and energy-conversion technologies.

Acknowledgments

This work was supported by the Research Grants Council of Hong Kong (grant no. CityU 21203518 and F-CityU106/18), Innovation and Technology Fund (grant no. MHP/104/21), City University of Hong Kong (grant no. 7005289, 7005580, 7005720, 9667213, 9667229, 9680331 and 9678291), Shenzhen Science Technology and Innovation Commission (grant no. JCYJ20210324125612035, R-IND12303 and R-IND12304), National Natural Science Foundation of China (Grant No. 22071070 and 51701159), and the U.S. National Science Foundation (CBET-2109842).

Appendix A. Supporting Information

The detailed description of time-resolved photoluminescence measurement using the FluoroLog including the equation in describing decay kinetics was fitted to a bi-exponential decay function (i.e., Eq. A·1 and Eq. A·2) and Table A·I.

Table I. Photovoltaic parameters of BP/$MAPbI_3$-based perovskite solar cells.

Molar ratio of BP/$MAPbI_3$	I_{sc} (mA cm^{-2})	V_{oc} (V)	FF	Efficiency (%)
0%	23.1	1.04	0.71	17.057
2%	23.7	1.05	0.768	19.112
4%	21.1	1.02	0.63	13.559
6%	20.5	0.98	0.465	9.342
8%	19.4	0.97	0.460	8.656
10%	17.6	0.92	0.401	6.493

ORCID

Hsien-Yi Hsu https://orcid.org/0000-0001-5931-271X

References

1. H.-Y. Hsu, L. Ji, H. S. Ahn, J. Zhao, E. T. Yu, and A. J. Bard, *J. Am. Chem. Soc.*, **137**, 14758 (2015).
2. C. H. Mak, X. Huang, R. Liu, Y. Tang, X. Han, L. Ji, X. Zou, G. Zou, and H.-Y. Hsu, *Nano Energy*, **73**, 104752 (2020).
3. X. Zou, L. Ji, H.-Y. Hsu, K. Zheng, Z. Pang, and X. Lu, *J. Mater. Chem. A*, **6**, 12724 (2018).
4. H.-Y. Hsu, L. Ji, C. Zhang, C. H. Mak, R. Liu, T. Wang, X. Zou, S.-Y. Leu, and E. T. Yu, *J. Mater. Chem. C*, **6**, 11552 (2018).
5. R. Liu, C. H. Mak, X. Han, Y. Tang, G. Jia, K.-C. Cheng, H. Qi, X. Zou, G. Zou, and H.-Y. Hsu, *J. Mater. Chem. A*, **8**, 23803 (2020).
6. Y. Li, L. Ji, R. Liu, C. Zhang, C. H. Mak, X. Zou, H.-H. Shen, S.-Y. Leu, and H.-Y. Hsu, *J. Mater. Chem. A*, **6**, 12842 (2018).
7. M. Kim, J. Jeong, H. Lu, T. K. Lee, F. T. Eickemeyer, Y. Liu, I. W. Choi, S. J. Choi, Y. Jo, and H.-B. Kim, *Science*, **375**, 302 (2022).
8. G. Niu, X. Guo, and L. Wang, *J. Mater. Chem. A*, **3**, 8970 (2015).
9. H. Y. Hsu, H. H. Hsieh, H. Y. Tuan, and J. L. Hwang, *Sol. Energy Mater. Sol. Cells*, **94**, 955 (2010).
10. C. H. Mak, X. Han, M. Du, J.-J. Kai, K. F. Tsang, G. Jia, K.-C. Cheng, H.-H. Shen, and H.-Y. Hsu, *J. Mater. Chem. A*, **9**, 4454 (2021).
11. C. Dong, Y. Wang, H. Wang, C. S. K. Lin, H. Y. Hsu, and S. Y. Leu, *Energy Procedia*, **158**, 918 (2019).
12. Y. Tang, C. H. Mak, R. Liu, Z. Wang, L. Ji, H. Song, C. Tan, F. Barrière, and H. Y. Hsu, *Adv. Funct. Mater.*, **30**, 2006919 (2020).
13. N. Arora, M. I. Dar, A. Hinderhofer, N. Pellet, F. Schreiber, S. M. Zakeeruddin, and M. Grätzel, *Science*, **358**, 768 (2017).
14. J. Zhao, H. Yin, T. Lim, H. Xie, H.-Y. Hsu, F. Forouzan, and A. J. Bard, *J. Electrochem. Soc.*, **163**, D506 (2016).
15. T.-H. Lai, I. Constantinou, C. M. Grand, E. D. Klump, S. Baek, H.-Y. Hsu, S.-W. Tsang, K. S. Schanze, J. R. Reynolds, and F. So, *Chem. Mater.*, **28**, 2433 (2016).
16. Y. Peng et al., *J. Mater. Chem. A*, **9**, 26628 (2021).
17. S. Rao, X. Zou, S. Wang, T. Shi, Y. Lu, L. Ji, H.-Y. Hsu, Q. Xu, and X. Lu, *J. Electrochem. Soc.*, **166**, D427 (2019).
18. S. S. Shin, E. J. Yeom, W. S. Yang, S. Hur, M. G. Kim, J. Im, J. Seo, J. H. Noh, and S. I. Seok, *Science*, **356**, 167 (2017).
19. W. Peng, X. Miao, V. Adinolfi, E. Alarousu, O. El Tall, A. H. Emwas, C. Zhao, G. Walters, J. Liu, and O. Ouellette, *Angew. Chem. Int. Ed.*, **55**, 10686 (2016).
20. C. H. Mak, R. Liu, X. Han, Y. Tang, X. Zou, H. H. Shen, Y. Meng, G. Zou, and H. Y. Hsu, *Adv. Opt. Mater.*, **8**, 2001023 (2020).
21. A. G. Ricciardulli, S. Yang, N. B. Kotadiya, G. J. A. Wetzelaer, X. Feng, and P. W. Blom, *Adv. Electron. Mater.*, **5**, 1800687 (2019).
22. I. Constantinou, T. H. Lai, H. Y. Hsu, S. H. Cheung, E. D. Klump, K. S. Schanze, S. K. So, and F. So, *Adv. Electron. Mater.*, **1**, 1500167 (2015).
23. W. Chen, K. Li, Y. Wang, X. Feng, Z. Liao, Q. Su, X. Lin, and Z. He, *The journal of physical chemistry letters*, **8**, 591 (2017).
24. Y. Wei and R. Long, *The journal of physical chemistry letters*, **9**, 3856 (2018).
25. Z. Chen, H.-Y. Hsu, M. Arca, and K. S. Schanze, *J. Phys. Chem. B*, **119**, 7198 (2014).
26. L. Bai, L. Sun, Y. Wang, Z. Liu, Q. Gao, H. Xiang, H. Xie, and Y. Zhao, *J. Mater. Chem. A*, **5**, 8280 (2017).
27. H. Y. Hsu, L. Ji, M. Du, J. Zhao, T. Y. Edward, and A. J. Bard, *Electrochim. Acta*, **220**, 205 (2016).
28. H. Y. Hsu, L. Ji, M. Du, J. Zhao, E. T. Yu, and A. J. Bard, *The Journal of Physical Chemistry C*, **120**, 19890 (2016).
29. J. H. Im, C. R. Lee, J. W. Lee, S. W. Park, and N. G. Park, *Nanoscale*, **3**, 4088 (2011).
30. Y. Zhao and K. Zhu, *The Journal of Physical Chemistry C*, **118**, 9412 (2014).
31. J. Lee, H. Ye, S. Pan, and A. J. Bard, *Anal. Chem.*, **80**, 7445 (2008).
32. X. Xu, C. Ma, Y. Cheng, Y. M. Xie, X. Yi, B. Gautam, S. Chen, H. W. Li, C. S. Lee, and F. So, *J. Power Sources*, **360**, 157 (2017).
33. J. L. Fernández, N. Mano, A. Heller, and A. J. Bard, *Angew. Chem.*, **116**, 6515 (2004).
34. K. Barman, X. Wang, R. Jia, and M. V. Mirkin, *J. Am. Chem. Soc.*, **143**, 8547 (2021).
35. R. G. Mariano, M. Kang, O. J. Wahab, I. J. McPherson, J. A. Rabinowitz, P. R. Unwin, and M. W. Kanan, *Nat. Mater.*, **20**, 1000 (2021).
36. J. L. Fernández, N. Mano, A. Heller, and A. J. Bard, *Angew. Chem. Int. Ed.*, **43**, 6355 (2004).
37. N. Mano, H.-H. Kim, and A. Heller, *J. Phys. Chem. B*, **106**, 8842 (2002).
38. K. C. Leonard, K. M. Nam, H. C. Lee, S. H. Kang, H. S. Park, and A. J. Bard, *The Journal of Physical Chemistry C*, **117**, 15901 (2013).
39. Y. Wang, H. Zhang, T. Zhang, W. Shi, M. Kan, J. Chen, and Y. Zhao, *Sol. RRL*, **3**, 1900197 (2019).
40. C. C. Stoumpos, C. D. Malliakas, and M. G. Kanatzidis, *Inorg. Chem.*, **52**, 9019 (2013).
41. S. D. Stranks, G. E. Eperon, G. Grancini, C. Menelaou, M. J. Alcocer, T. Leijtens, L. M. Herz, A. Petrozza, and H. J. Snaith, *Science*, **342**, 341 (2013).
42. N. Pellet, P. Gao, G. Gregori, T. Y. Yang, M. K. Nazeeruddin, J. Maier, and M. Grätzel, *Angew. Chem. Int. Ed.*, **53**, 3151 (2014).
43. C. S. Ponseca et al., *J. Am. Chem. Soc.*, **136**, 5189 (2014).
44. T. C. Sum and N. Mathews, *Energy Environ. Sci.*, **7**, 2518 (2014).
45. D. Song et al., *The Journal of Physical Chemistry C*, **119**, 22812 (2015).
46. G. Xing, N. Mathews, S. Sun, S. S. Lim, Y. M. Lam, M. Grätzel, S. Mhaisalkar, and T. C. Sum, *Science*, **342**, 344 (2013).
47. Q. Chen, H. Zhou, T.-B. Song, S. Luo, Z. Hong, H.-S. Duan, L. Dou, Y. Liu, and Y. Yang, *Nano Lett.*, **14**, 4158 (2014).
48. M. Hadadian, J. P. Correa-Baena, E. K. Goharshadi, A. Ummadisingu, J. Y. Seo, J. Luo, S. Gholipour, S. M. Zakeeruddin, M. Saliba, and A. Abate, *Adv. Mater.*, **28**, 8681 (2016).
49. R. Long, W. Fang, and A. V. Akimov, *The journal of physical chemistry letters*, **7**, 653 (2016).
50. Y. Deng, Z. Luo, N. J. Conrad, H. Liu, Y. Gong, S. Najmaei, P. M. Ajayan, J. Lou, X. Xu, and P. D. Ye, *ACS nano*, **8**, 8292 (2014).